3T Eulerian-radiation description of graphite laser induced plasma under Martian conditions

K. Benbaier, A. Abdelmalek and Z. Bedrane
Theoretical Physics Laboratory, Physics Dpt., Sciences Faculty, Tlemcen University, Algeria.

Received 30 April 2024; accepted 5 July 2024

We report the results of a simulation of the laser-induced breakdown spectra of graphite in an atmosphere similar to that of Mars using a non-equilibrium 3T-Eurlian fluid model. In our approach the atomic energy level populations were calculated using a collisional-radiative (CR) NLTE-model taking into account the mixing between the plasma and the ambiant gas. The simulation was performed with the FLASH radiation-hydrodynamics code. We have investigate the effects of laser irradiance and ambient CO_2 pressure on the plasma parameters namely the electron and ion temperatures and the electron and ion densities and the temporal variation of the fluid velocity with the laser irradiance at constant pressure which indicate the presence of a shock front associated with the plasma initiation, dynamics, and expansion into the ambient gas.

Keywords: 3T-Eurlian model; NLTE; LIBS; mars; plasma physics.

DOI: https://doi.org/10.31349/RevMexFis.71.011501

1. Introduction

For centuries, the planet Mars has exerted a kind of fascination on humans. But if astronomers today are so interested in the Red Planet, it is primarily because of its relative proximity makes it reachable to their probes and other rovers. Moreover, unlike the other planets of the Solar System, Mars undoubtedly experienced in the past conditions quite similar to those prevailing on Earth which could have allowed the appearance of life - which remains to be confirmed [1].

Nasa Space missions steadily advanced our knowledge of the planet. The main scientific goal of the Nasa's Exploration Program studies is to understand the formation and early evolution of Mars as a planet, the history of geological processes that have shaped Mars through time, the potential for Mars to have hosted life, and the future exploration of Mars by humans [1].

Laser Induced Breakdown Spectroscopy (LIBS) has made it possible to analyze numerous geological samples on the surface of the Martian soil since 2012 thanks to the ChemCam instrument installed on board the Curiosity rover, the largest and most capable rover ever sent to Mars and which has already carried out more than a million laser shots. ChemCam is based on the technique of spectroscopic analysis induced by laser ablation. A powerful laser fires on a target, which causes the volatilization of the material and the appearance of a plasma whose fluorescence is analyzed [2]. Building on this success, LIBS was once again chosen by NASA to be one of the analysis tools implemented by the SuperCam instrument, installed on board the Perseverance rover, which reached the Martian soil in February 2021 [3].

In an effort to better understand ChemCam LIBS spectra numerical simulations in an approach complementary to that based on mimicking the experimental conditions on Mars in an Earth-based laboratory [4] has been performed [5–9]. Ewusi-Annan *et al*. [8] reported the results of a simulation of the laser-induced breakdown spectra of graphite and synthetic shergottite glass in an atmosphere similar to that of Mars using a 1-D, Lagrangian hydrodynamic model and a local thermodynamic equilibrium (LTE) approach for the emission spectra.

Hansen *et al*. [9] investigated the characteristics of the LIBS plasma in Martian atmospheric conditions using stationary modeling of the LIBS plasma using a one-dimensional model of the plasma divided into two zones along the line of sight. Their simulations were based on local thermal equilibrium and carried out using radiative transfer.

Most approaches for characterizing the LIBS plasma are based on the assumption of local thermodynamic equilibrium (LTE) due to the simplicity of the description of the plasma in LTE although the validity of this assumption can only be considered under certain experimental conditions at specific time intervals after plasma initiation [9, 10].

In a recent work, Alberti *et al*. [11] used a non-equilibrium model for laser generated plasmas to investigate plasma kernel dynamics. Laser-induced plasma simulations were performed for nanosecond length pulses for a range of ambient conditions and laser characteristics, and were able to correctly predict the axial and radial sizes of the plasma and, more importantly, to reproduce the propagation of the forward and backward plasma waves observed in experiments in air [12] and Argon [13].

In this paper, we present a novel simulation to model the problem of laser-induced breakdown spectroscopy under Martian conditions . This includes a three temperature (3T) Eurlian radiation description with NLTE (non-local thermodynamic equilibrium) approach for the emission spectra. To model the laser target interaction in the presence of an ambient gas, the usual two temperature (2T) model [14] treatment of plasma is not sufficient since there are a number of physical processes that cause a deviation from electron-

ion radiation thermal equilibrium, or which are critically affected, such as laser heating, transport coefficients, shock waves generation, diffusion effect of radiation, radiation absorption, emission from the plasma and slow equilibration timescales. In order to include these effects, we have considered a 3T plasma model. The simulation was performed with the FLASH radiation-hydrodynamics code [15] which is a finite-volume Eulerian code that operates on a block-structured mesh using Adaptive Mesh Refinement (AMR) [16].

The term "three-temperature" (or "3T") denotes the approximation that electrons and ions move together as a single fluid but with two different temperatures, and that this fluid can emit or absorb radiation. In the 3T simulations presented throughout this paper each cell has an electron temperature, an ion temperature, and radiation energy densities in a number of photon energy bins [17]. In our approach the atomic energy level populations were calculated using a collisional-radiative (CR) NLTE-model [18]. The plasma simulations were allowed to evolve for different times utilizing the second-order unsplit time marching method of USM algorithm [19], an extension of the corner transport upwind (CTU) approach [20] reconstruction was done utilizing the piecewise monotonized central (MC) limiter. The upwind fluxes were computed with a Harten-Laxvan Leer Contact (HLLC) Riemann solver [21]. Implicit solvers for radiation and electron thermal conduction was carried out using a conjugate gradient method (PCG), preconditioned with algebraic multi-grid (AMG), as implemented in the HYPRE library [22].

2. Modeling approach

2.1. Hydrodynamics and plasma radiation simulation

The Euler equations expressing conservation of mass, momentum, and total energy used to describe the evolution of a hydrodynamics 3T plasma are given by [23, 24]:

$$\frac{\partial \rho}{\partial t} + \nabla.(\rho \overrightarrow{v}) = 0, \tag{1}$$

$$\frac{\partial}{\partial t}(\rho \overrightarrow{v}) + \nabla.(\rho \overrightarrow{v}\,\overrightarrow{v}) + \nabla P_{\rm tot} = 0, \tag{2}$$

$$\frac{\partial}{\partial t}(\rho \overrightarrow{v}) + \nabla.[(\rho E_{\rm tot} + P_{\rm tot})\overrightarrow{v}] = Q_{\rm las} - \nabla.\overrightarrow{q}, \tag{3}$$

where

$$P_{\rm tot} = P_{\rm ele} + P_{\rm ion} + P_{\rm rad}, \tag{4}$$

$$E_{\rm tot} = e_{\rm ele} + e_{\rm ion} + e_{\rm rad} + \frac{1}{2}\overrightarrow{v}\,\overrightarrow{v}. \tag{5}$$

Here ρ is the plasma mass density, $\overrightarrow{v}$ is the fluid velocity, $P_{\rm tot}$ is the total pressure, $P_{\rm ele}$, $P_{\rm ion}$ and $P_{\rm rad}$ are the electron, the ion and the radiation pressure, respectively. $E_{\rm tot}$ is the total specific energy which includes the specific internal energies of the electron $e_{\rm ele}$, ions $e_{\rm ion}$ and the radiation field $e_{\rm rad}$ along with the specific kinetic energy. $Q_{\rm las}$ is the energy source due to laser heating. $\overrightarrow{q}$ is the total heat flux which is the sum of the electron, the ion heat flux and the radiation flux:

$$\overrightarrow{q} = \overrightarrow{q}_{\rm ele} + \overrightarrow{q}_{\rm ion} + \overrightarrow{q}_{\rm rad}, \tag{6}$$

$$\overrightarrow{q}_{\rm ele} = -K_{\rm ele}\nabla.T_{\rm ele}, \tag{7}$$

$$\overrightarrow{q}_{\rm ion} = -K_{\rm ion}\nabla.T_{\rm ion}, \tag{8}$$

where $K_{\rm ele}$ and $K_{\rm ion}$ are respectively the electron and the ion thermal conductivity which are determined using the Spitzer model [25, 26]. In cases where a large values of $|\nabla.T_{\rm ele}|$ and $|\nabla.T_{\rm ion}|$ would give rise to unphysically large heat fluxes, this can be handled by the diffusion flux-limiter solver. The maximum flux-limit used for electron $\overrightarrow{q}_{\max_{\rm ele}}$, ion $\overrightarrow{q}_{\max_{\rm ion}}$ thermal conductions, respectively are defined as [15]:

$$\overrightarrow{q}_{\max_{\rm ele(ion)}} = \alpha_{\rm e(i)} n_{\rm e(i)} k_{\rm B} T_{\rm ele(ion)} \sqrt{\frac{k_{\rm B} T_{\rm ele(ion)}}{m_{\rm e(i)}}}, \tag{9}$$

where $k_{\rm B}$ is the Boltzmann constant, $m_{\rm i}$ is the average mass of an ion, $m_{\rm e}$ is the mass of electron, $n_{\rm e}$ is the electron density, $n_{\rm i}$ is the ion density. $\alpha_{\rm e}$ and $\alpha_{\rm e}$ are respectively the electron and the ion conductivity flux-limiter coefficient. This coefficients are much less than 1 [26].

Since the plasma is assumed to have multi-temperatures, additional equations must be evolved to describe the change in specific internal energies of the ions, electrons, and radiations field:

$$\frac{\partial \rho e_{\rm ion}}{\partial t} + \nabla.(\rho e_{\rm ion}\overrightarrow{v}) + P_{\rm ion}\nabla.\overrightarrow{v} = \rho\omega_{\rm ei}(T_{\rm ele} - T_{\rm ion}) - \nabla.\overrightarrow{q}_{\rm ion}, \tag{10}$$

$$\frac{\partial \rho e_{\rm elec}}{\partial t} + \nabla.(\rho e_{\rm elec}\overrightarrow{v}) + P_{\rm ele}\nabla.\overrightarrow{v} = \rho\omega_{\rm ei}(T_{\rm ion} - T_{\rm ele}) - \nabla.\overrightarrow{q}_{\rm ele} + Q_{\rm abs} - Q_{\rm emis} + Q_{\rm las}, \tag{11}$$

$$\frac{\partial \rho e_{\rm rad}}{\partial t} + \nabla.(\rho e_{\rm rad}\overrightarrow{v}) + P_{\rm rad}\nabla.\overrightarrow{v} = -\nabla.\overrightarrow{q}_{\rm rad} - Q_{\rm abs} + Q_{\rm emis}, \tag{12}$$

where $e_{\rm ion}$ is the ion specific internal energy, $e_{\rm ele}$ is the electron specific internal energy, $e_{\rm rad}$ is the radiation specific internal energy. $Q_{\rm las}$ is represents the energy source due to laser heating. $Q_{\rm abs}$ represents the increase in electron internal energy due to the total absorption of radiation, $Q_{\rm emis}$ represents the decrease in electron internal energy due to the total emission of radiation.

Where $\omega_{\rm ei} = C_{v,e}/\tau_{\rm ei}$ is the electron-ion coupling term, where $C_{v,e}$ is the electron specific heat and $\tau_{\rm ei}$ is the ion/electron equilibration time given by [26]:

$$\tau_{\rm ei} = \frac{3k_{\rm B}^{3/2}}{8\sqrt{2\pi}q_{\rm e}^4}.\frac{(m_{\rm i}T_{\rm ele} + m_{\rm e}T_{\rm ion})^{3/2}}{(m_{\rm e}m_{\rm i})^{1/2}\overline{Z}n_{\rm i}\ln\Lambda_{\rm ei}}, \tag{13}$$

where $\overline{Z}$ is the average ionization, $n_{\rm i}$ the ionic density, $q_{\rm e}$ the electron charge and $\ln \Lambda_{\rm ei}$ is the Coulomb Logarithm associated to the ion-electron collisions [27].

FLASH code already provides a variety of directionally split and unsplit methods for solving the system of Euler equations of hydrodynamics (HD). The system of Eqs. (1), (2), (3) is a mixed hyperbolic-parabolic system. First, all the terms on the right-hand side of the equations are split off from the solution of the non- ideal single-fluid hydrodynamics. The latter is handled using the single step, time marching algorithm of the unsplit staggered mesh (USM) [19, 31] for cartesian coordinates. The right-hand terms of Eqs. (10), (11), (12) is in turn split off and each term is handled separately. The first term on the right-hand side Eqs. (10), (11) represents the exchange of energy between electrons and ions through collisions, and it is handled by solving the system as [15]:

$$\frac{\partial e_{\rm ion}}{\partial t} = \frac{C_{v,\rm elec}}{\tau_{\rm ei}}(T_{\rm ele} - T_{\rm ion}), \tag{14}$$

$$\frac{\partial e_{\rm ele}}{\partial t} = \frac{C_{v,\rm elec}}{\tau_{\rm ei}}(T_{\rm ion} - T_{\rm ele}). \tag{15}$$

The second term on the right-hand side of Eqs. (14) and (15) represents the electron thermal conduction and the parabolic terms, which are solved implicitly using the HYPRE library [22], to retain large time steps.

The remaining terms on the right-hand of Eqs. (11) and (12) describe radiation transport. The HYPRE library was used to calculate the radiation diffusion.

FLASH code includes radiative transfer through the following equation:

$$\frac{1}{c}\frac{\partial I}{\partial t} + \widehat{\Omega}.\nabla I + \rho\kappa I = \eta, \tag{16}$$

where $I(x, \widehat{\Omega}, \nu, t)$ is the specific radiation intensity at position x in the direction $\widehat{\Omega}$, c is the speed of the light, ρ is the mass density $\kappa(x, \nu, t)$ is the opacity or absorption coefficient, $\eta(x, \nu, t)$ is the emissivity, ν is the frequency. This equation is coupled within FLASH to the electron internal energy through:

$$\frac{\partial u_{\rm ele}}{\partial t} = \int_O^\infty d\nu \int_{4\pi} d\widehat{\Omega}(\rho\kappa I - \eta), \tag{17}$$

where $u_{\rm ele} = \rho.e_{\rm ele}$ represent the electron internal energy density, $e_{\rm ele}$ is the internal electron energy, and ρ the total mass density.

The radiative transfer Eq. (16), and the electron internal energy Eq. (17) equations are handled using multi-group diffusion (MGD) approximation [32]. FLASH divided the frequency space into N groups, where g is defined by the frequency range from ν_g to ν_{g+1}. For our Simulation the number of frequency groups used is 25, and the total quantities of interest can be defined as summations over each group:

$$Q_{\rm emis} = \sum_{g=1}^{N_g} Q_{\rm emis,g}, \tag{18}$$

$$Q_{\rm abs} = \sum_{g=1}^{N_g} Q_{\rm abs,g}, \tag{19}$$

$$Q_{\rm rad} = \sum_{g=1}^{N_g} Q_{\rm rad,g}, \tag{20}$$

$$u_{\rm rad} = \sum_{g=1}^{N_g} u_{\rm rard,g}, \tag{21}$$

where $u_{\rm rad} = \rho e_{\rm rad}$ is the radiation energy density, where $e_{\rm rad}$ is the internal radiation energy.

The total energy density is given by:

$$\begin{aligned}\varepsilon &= \rho.E_{\rm tot} = \rho.E_{\rm internal} + \rho.E_{\rm kinetic} \\ &= \rho.(e_{\rm ele} + e_{\rm ion} + e_{\rm rad}) + \frac{1}{2}\rho.\overrightarrow{v}\overrightarrow{v}.\end{aligned} \tag{22}$$

Then we solve the following system of equations, assuming that the plasma emitted a radiation in a Planck spectrum with an emission opacity given by:

$$\begin{aligned}\frac{1}{c}\frac{\partial u_{\rm rad}}{\partial t} - \nabla.\left(\frac{1}{3\sigma_{\rm t,g}}\nabla u_{\rm rad}\right) + \sigma_{\rm a,g}u_{\rm rad} \\ = \sigma_{\rm e,g}aT_{\rm ele}^4\frac{15}{\pi^4}\left[P(x_{\rm g+1}) - P(x_{\rm g})\right],\end{aligned} \tag{23}$$

$$\begin{aligned}\frac{\partial u_{\rm ele}}{\partial t} = \sum_{\rm g}\Bigg(\sigma_{\rm a,g}u_{\rm rad} - \sigma_{\rm e,g}aT_{\rm ele}^4 \\ \times \frac{15}{\pi^4}\left[P(x_{\rm g+1}) - P(x_{\rm g})\right]\Bigg),\end{aligned} \tag{24}$$

where $u_{\rm rad}$ is the radiation energy density, $\sigma_{\rm t,g}$ is the transport opacity for group g, $\sigma_{\rm a,g}$ is the absorption opacity for group g, $\sigma_{\rm e,g}$ is the emission opacity for group g, a is the radiation constant, and $P(x)$ is the Planck integral. The argument to the Planck integral is $x = h\nu/kT$ where h is the Planck's constant. The second and third terms on the left-hand side of equation Eq. (23) represent $\nabla Q_{\rm rad,g}$ and $Q_{\rm abs,g}$, respectively. While the right-hand side of Eq. (23) represent $Q_{\rm emis,g}$.

The last term of Eq. (11) represents the laser heating $Q_{\rm las,g}$, which is computed using an inverse Bremsstrahlung model (described in Appendix A). The energy deposited by the laser beam was calculated using the laser ray-trace algorithm for planar and cylindrical geometries. This algorithm was used by FLASH to calculates the paths of each rays using the geometric optics approach [33]. Beams are the collection of a number of rays whose paths are traced through the simulation domain based on the local index of refraction of each cell. The power of the laser deposited in a cell is assumed to be due to the inverse Bremsstrahlung power, which depends on the electron temperature gradient and the electron number

density gradient. The ion number density $n_{\rm i}$ and the electron number density $n_{\rm e}$ of our work were obtained from the following equations [15]:

$$n_{\rm i} = N_{\rm A}\frac{\rho}{\overline{A}}, \tag{25}$$

$$n_{\rm e} = N_{\rm A}\overline{Z}\frac{\rho}{\overline{A}}, \tag{26}$$

where $N_{\rm A}$ is the Avogadro number, $\overline{A}$ is the average atomic mass, $\overline{Z}$ is the average ionization level, and ρ is the mass density.

2.2. Simulation code

The software used in our work is the FLASH Code [28]. It is a multi-physics, multi-dimensional radiation-hydrodynamic, and magneto-hydrodynamic (MHD) open-source code capable of handling different physics problems like plasma emission phenomena. Flash has also extensive high energy density plasmas (HEDP) capabilities for simulating laser-driven plasma experiments [29], and a variety of partial differential equations (PDE) solver employed in the numerical modeling. By a range of algorithms FLASH include adaptive mesh refinement capabilities (AMR) [30]. This means that the grid includes individual blocks which can be divided into smaller blocks (children blocks), providing a better resolution in desired regions of the domain. The refinement can be triggered by a chosen variables, such as density or temperature. In our simulation we used 4 refinement variables: density, electron temperature, ion temperature and pressure. Unlike Lagrangian hydrodynamics code [8] where the mesh moves with the fluid, FLASH code utilizes an Eulerian representation of the fluid, where the stationary spatial mesh allows fluid to move into and out of a cell, this gives FLASH the feature of avoiding mesh entanglement, to handed multi-complex fluid. HEDP capabilities includes range of algorithms: three temperatures (electron, ion, and radiation) state-of-the art radiation-hydrodynamics solver, including the thermal conduction, multi-group radiation diffusion, tabulated equations-of states, and laser ray-tracing model. The laser ray-tracing model is in 1D, 2D, and 3D Cartesian coordinates and in 2D cylindrical coordinate.

2.3. Equations of State (EOS) and opacities

The equations of state (EOS) for the target (Graphite) and ambient gas (CO_2) were used in the computation for the electrons, ions and radiation pressures ($P_{\rm ele}$, $P_{\rm ion}$, $P_{\rm rad}$), the electron and ion specific heats ($C_{v,{\rm ele}}$, $C_{v,{\rm ion}}$), electron, ion and radiation internal energies ($e_{\rm ele}$, $e_{\rm ion}$, $e_{\rm rad}$) and electron-ion coupling term ($\omega_{\rm ei}$) from the plasma temperature and ion density grid. To compute tabulated EOS for NLTE plasma we used the program IONMIX4 [18]. The IONMIX4 code was also used to calculate tabulated emissivity and opacity for NLTE used by FLASH code.

The IONMIX code computes the steady-state ionization and excitation populations for a mixture of up to 10 different atomic species. The radiative absorption, emission, and scattering coefficients are calculated at a large number ($\sim$ several hundred) of photon energies, and integrated over selected energy intervals to determine the multi-group Planck and Rosseland mean opacities. The code also calculates the thermodynamic properties of the plasma, such as the specific energy, average charge state, pressure, and heat capacity [18].

A temperature grid spanning 0.01-50 eV, ion density grid in the range of 10^{12}-10^{25} ion/cm^3 and an energy grid from 1 to 6 eV were used in the calculation of the EOS and opacity data respectively. The ionization potential energies of the excited levels for carbon (C^{+1}, C^{+2}, C^{+3}, C^{+4}, C^{+5}, C^{+6}) and oxygen (O^{+1}, O^{+2}, O^{+3}, O^{+4}, O^{+5}, O^{+6}, O^{+7}, O^{+8}) were driven from the National Institute of Science and Technology (NIST) [34] and used by IONMIX4 to generate data for the Graphite and Carbon dioxide (CO_2). The populations of atomic energy levels were calculated using a collisional-radiatif non-local thermodynamic equilibrium (CR-NLTE) model [18] (described in Appendix B). It should be noted that in our simulation, the emission from molecules has not been considered. Experimental evidence [35] confirms the presence of molecules in the graphite plasma beyond a delay time of 1 μs. This suggests that the emission line intensities of atomic species could be influenced by molecular formation throughout the plasma's duration. Notably, our simulation accounts for a duration of only up to 1000 ns.

2.4. Design simulation setup

In order to simulate the ablation of the Graphite target and the plasma formation in presence of an ambient gas (CO_2), we took advantage of support for multi-materials in the FLASH Code. In our Simulation we have considered a 0.1 cm thick and 0.5 cm radius flat solid graphite ($\rho = 2.23$ g/cm^3) target irradiated by 1064 nm, 5 ns temporal "top-hat" shaped laser pulse (Fig. 1) with laser energy on the target $E_{\rm las} = 15$ mJ [36].

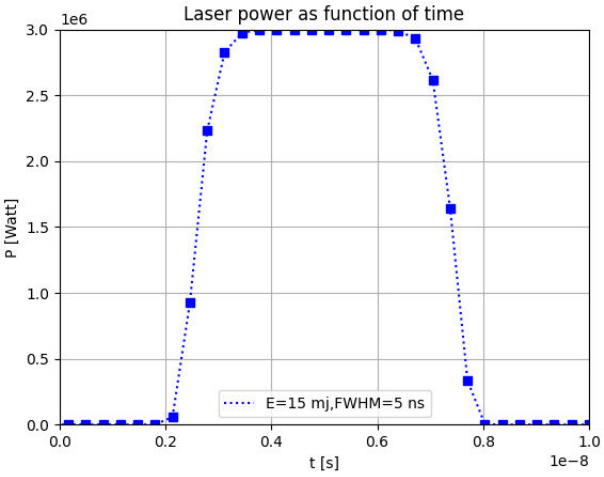

FIGURE 1. Top hat laser beam profile as function of time.

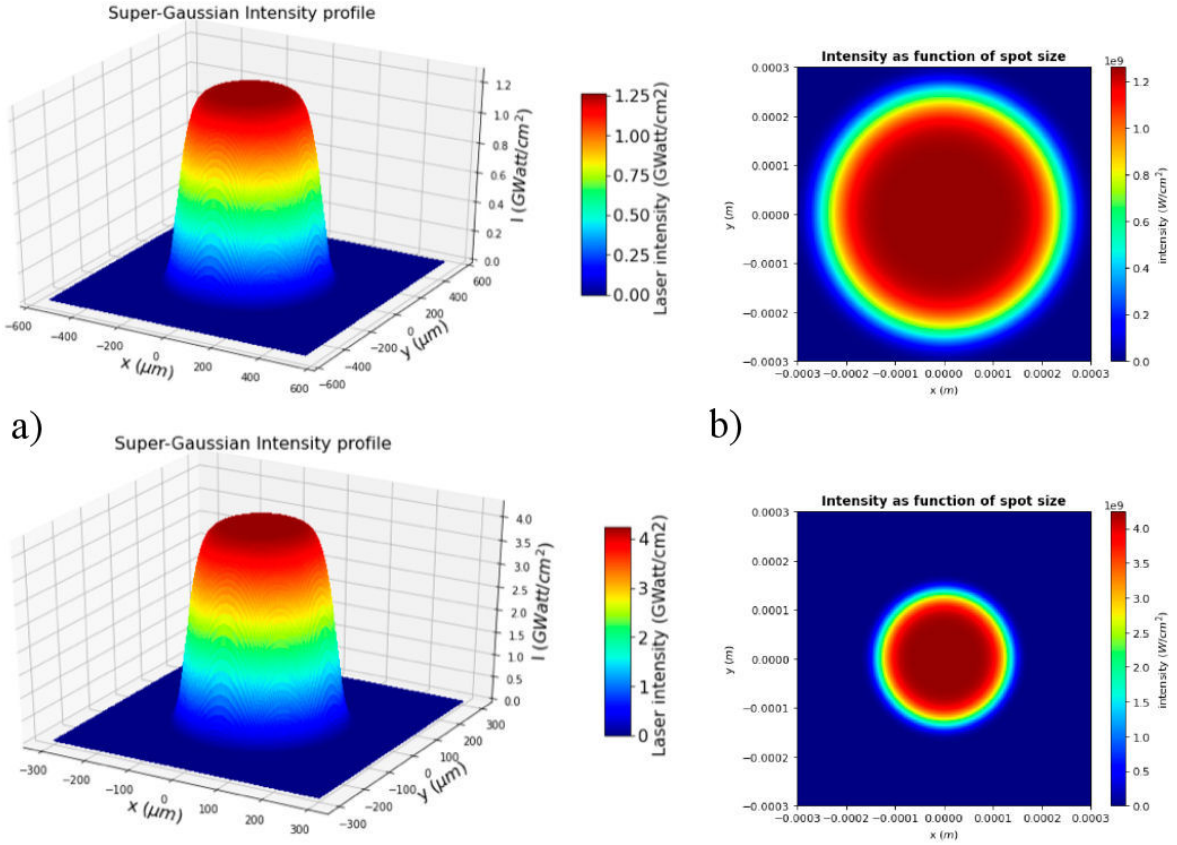

FIGURE 2. Super-Gaussian laser intensity profile a) and the laser intensity as function of the spot size b) are given for 1 GW/cm^2 (1$^{\rm st}$ row) and for 4 GW/cm^2 (2$^{\rm nd}$ row).

The spatial profile of the laser intensity was assumed to be a super-Gaussian of exponent 4 an e^2-folding radius, its expression is given by [37–39]:

$$I(r) = I_0 \mathrm{e}^{-2\left[(\frac{r}{\omega_0})^2\right]^n} \tag{27}$$

where I_0 is the laser intensity, n is the super Gaussian exponent selected to be 4 in our simulation, r is the radius, and ω_0 is the e^2-folding Gaussian radius for our laser set to 150 μm, 225 μm, respectively. Initially, the region of $y \geqslant 0.9$ cm occupied by the target (target thick = 1 mm, and target radius = 5 mm), and the region of $y < 0.9$ cm is assumed to be occupied by the ambient gas (CO_2) with different pressures (3 mbars, 6 mbars et 9 mbars). The large spatial extent of the atmosphere is chosen to mimic the distance between the laser source (ChemCam telescope), and the target on Mars which varies between 1 m (spot size diameter $D = 300$ μm) and 7 m (spot size diameter $D = 550$ μm) (Fig. 2).

In our simulation we used one of laser ray-tracing model proprieties in the FLASH Code, this allows to 2D Cartesian laser beam to emulate a 3D cylindrical beam. The plasma simulations are allowed to evolve for 100 ns, 500 ns and 1000 ns respectively, utilizing the unsplit staggered mesh (USM) scheme, a currant number of 0.1 the time step used in the simulation varied from 1 fs to 0.1 ns. We used 4 levels of refinement and blocks of 8 $\times$ 8 cells, obtaining an equivalent resolution of approximately 78 μm per cell. The reconstruction is carried out with a monotonized central (MC) limiter [40], whereas the Godunov fluxes are recovered with an HLLC Riemann solver [21, 41], which restores contact surface and cut wave. The boundary conditions were set to outflow for all axis.

For visualizing our data we have used the multi-code analysis tool "yt-project" [42], an open-source code written in Python which consists on data management layer for transporting and tracking simulation out-puts, plotting layer, parallel analysis layer for handling mesh-based and particle-based data as well as several interfaces, "yt" has been extended to work with several different simulation methods and simulation codes including FLASH code.

3. Results and discussion

3.1. Electron temperature

To calculate the electron and ion temperatures, we consider, in our simulation model, a single laser beam with 4096 rays illuminating a flat solid graphite target (radius = 0.05 cm, thickness=0.05 cm) in 2D-Cartesian geometry ($x - y$). The laser is focused on the y-axis, and enters $x \in [-0.5; 0.5\,\mathrm{cm}] \times y \in [-1; 1\,\mathrm{cm}]$ computational domain at a 0° angle, the ambient gas is supposed to be CO_2 (Fig. 3). The boundary conditions are set to outflow for all axes. We

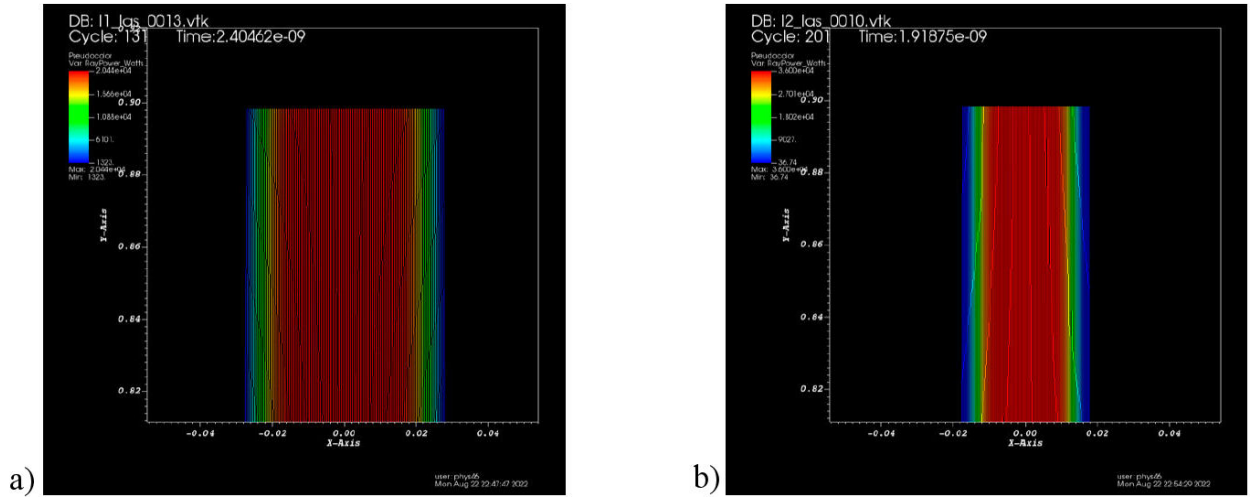

FIGURE 3. Laser beam simulated using 4096 rays per time step in 2D-Cartesian geometry $(x-y)$ a) for 1 GW/cm^2 and b) for 4 GW/cm^2.

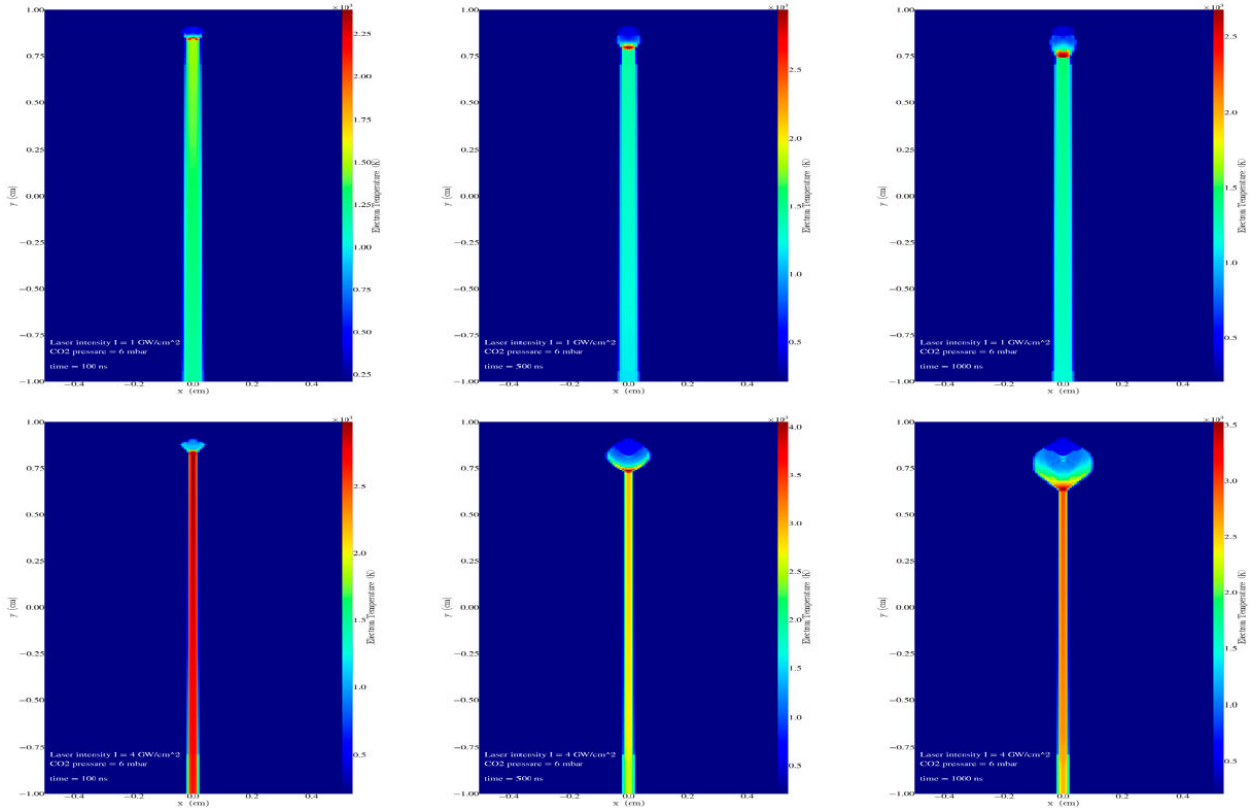

FIGURE 4. Electron temperature calculated at 6 mbars $C0_2$ ambient gas pressure, for 1 GW/cm^2, (1$^{\text{st}}$ row), 4 GW/cm^2 (2$^{\text{nd}}$ row) laser irradiance and for 3 time steps: 100 ns (1$^{\text{st}}$ column), 500 ns (2$^{\text{nd}}$ column) and 1000 ns (3$^{\text{rd}}$ column).

used 4 levels of refinement and blocks of 8×8 cells, obtaining an equivalent resolution of approximately 78 μm per cell.

Figure Fig. 4 shows the electron temperature for carbon dioxide pressure of 6 mbars and two laser irradiances 1 GW/cm^2 and 4 GW/cm^2 and three simulation times 100, 500 and 1000 ns. Each row in the figure shows the result obtained using one laser irradiance at 3 time steps. Each column shows the results for the same time for the two laser irradiances.

Both the electron and its spatial extent distribution are affected by the ambient gas pressure and the laser irradiance. At all simulation times the temperature increases with growing laser irradiance as obtained experimentally by Harilal *et al.* [43] when measuring the temperature in a laser produced carbon plasma. Figure 5 shows the influence of the laser irradiance on the maximum magnitude of the electron temperature for a constant pressure. The blue line correspond to 1 GW/cm^2 and the red line to 4 GW/cm^2.

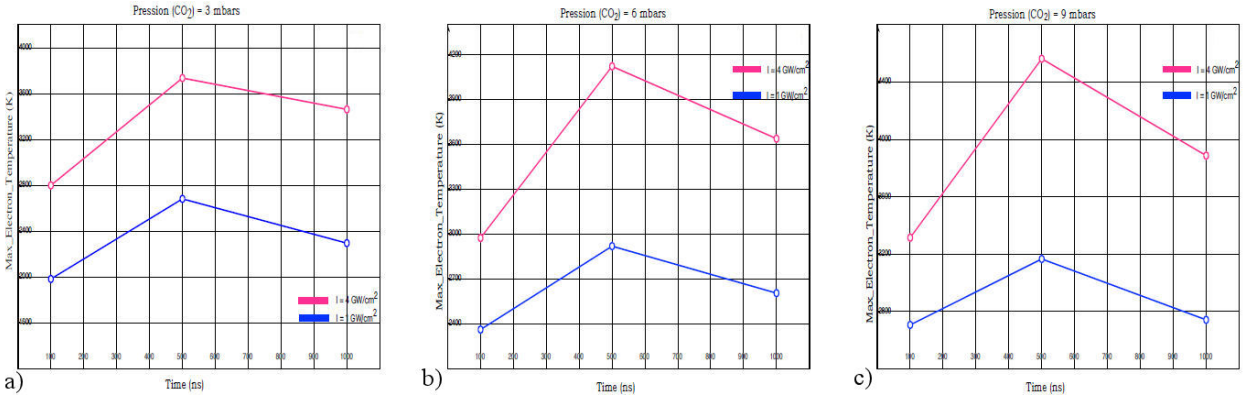

FIGURE 5. Influence of the laser irradiance (1 GW/cm^2 blue line, 4 GW/cm^2 red line) on the electron temperature for a constant pressure : a) 3 mbars, b) 6 mbars and c) 9 mbars.

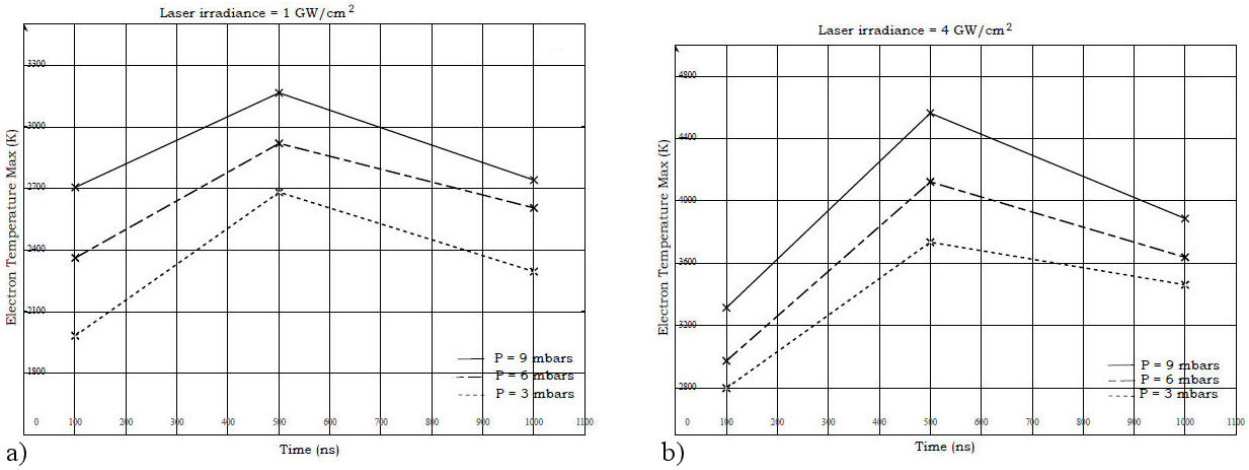

FIGURE 6. Variation of the electron temperature with the pressure (3 mbars dotted line, 6 mbars broken line and 9 mbars full line) at constant laser irradiance [a): 1 GW/cm^2, b) 4 GW/cm^2].

For a constant pressure, the magnitude of the temperature increases with laser irradiance at all time steps reaching a peak temperature at 500ns: increasing from 2681.2 K to 3735.4 K at 3 mbars, 2919.2 K to 4122.3 K at 6 mbars and 3165.4 K to 4563.0 K at 9 mbars when the laser irradiance increases fron 1 GW/cm^2 to 4 GW/cm^2 respectively, which represents an average increase of 1.4 of the magnitude of the electron temperature. We can notice that the spatial extent distribution is also affected and increases with growing laser irradiance.

Figure 6 shows the variation of the temperature with pressure which dependent on the laser irradiance and the time of observation.

At constant laser irradiance, the electron temperature increases slightly with growing ambiant pressure. At 4 GW/cm^2, the peak temperature at 500 ns varied from 3735.4 K at 3 mbars to 4122.3 K and 4563.0 K at 6 and 9 mbars, respectively. for the other time steps the augmentation is not very important ($\sim$175 K at 100 ns and $\sim$100 K at 1000 ns)

Overall, pressure effect on the electron temperature is marginal compared to the effect of laser irradiance.

What should be noted is that the temperature values we found are lower by a factor of 10 compared to those found by [8, 9]. The reason is that we considered in our simulation the real conditions on the planet Mars namely an average temperature of $-63°$ (initial temperature for graphite and CO_2) whereas experiments, carried out in Earth-based laboratory mimicking the experimental conditions on Mars, are carried out at room temperature [4, 6] or 0° which dramatically overestimates the temperature values [45]. Adding to this, we considered in our approach, the mixing between the plasma and the ambient gas which play an important role in the plasma plume expansion and affect the temperature and the density number of the plasma [46]. Moreover, the possible cause for the over-predicted values obtained by [8, 9] could be due to neglecting plasma emission and re-absorption in their 2T model and assuming the LTE. It is important to note that the EOS model controls not only the pressure of the plasma, given a density and temperature, but also affects the efficiency of heat conduction by determining the mean ionization fraction, as well as the specific heat [17, 44].

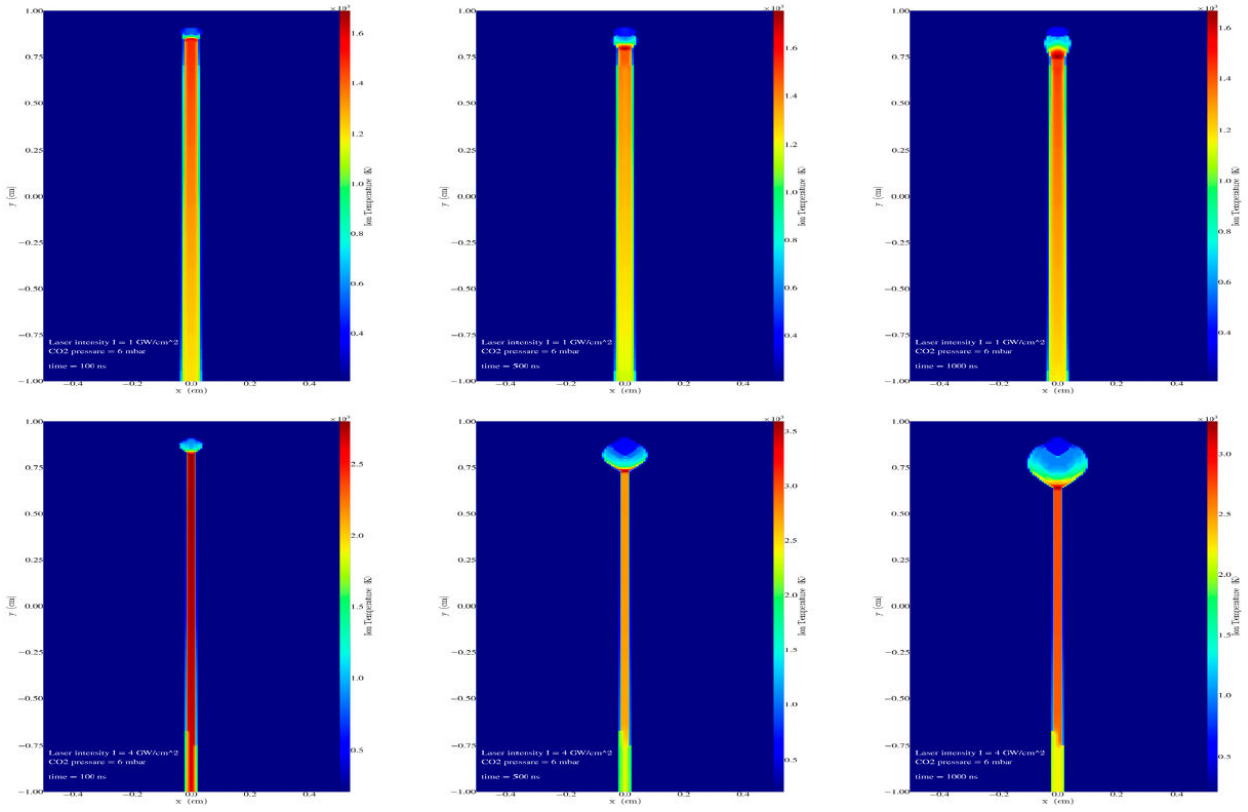

FIGURE 7. Ion temperature calculated at 6 mbars CO_2 ambient gas pressure, for 1 GW/cm^2, (1st row), 4 GW/cm^2 (2nd row) laser irradiance and for 3 time steps: 100 ns (1st column), 500 ns (2nd column) and 1000 ns (3rd column).

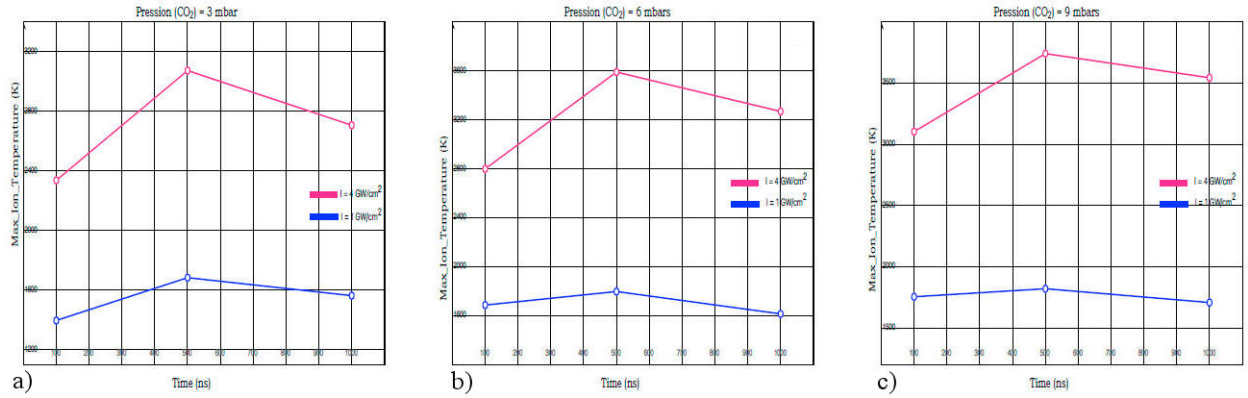

FIGURE 8. Influence of the laser irradiance (1 GW/cm^2 blue line, 4 GW/cm^2 red line) on the ion temperature for a constant pressure: a) 3 mbars, b) 6 mbars and c) 9 mbars.

3.2. Ion temperature

Figure 7 shows the electron temperature for carbon dioxide pressure of 6 mbars and two laser irradiances 1 GW/cm^2 and 4 GW/cm^2 and three simulation times 100, 500 and 1000 ns. Each row in the figure shows the result obtained using one laser irradiance at 3 time steps. Each column shows the results for the same time for the two laser irradiances.

Figure 8 shows the influence of the laser irradiance on the maximum magnitude of the ion temperature for a constant pressure. The blue line correspond to 1 GW/cm^2 and the red line to 4 GW/cm^2.

At 1 GW/cm^2 the ion temperature increases very slightly with time for the three pressures considered. At 6 mbars, for example, its varied from 1687.2 K at 100 ns to 1797.9 K and 1615.2 K at 500, 1000 ns, respectively. The evolution become more noticeable when the laser irradiance grows to 4 GW/cm^2 and even the magnitude grows significantly and reach a peak for 500 ns increasing from 1684.1 K to 3074.1 K at 3 mbars, 1797.9 K to 3591.2 K at 6 mbars and 1820.7 K to 3741.9 K at 9 mbars. The effect of the variation of the pressure on the ion temperature is not very important as shown in Fig. 9.

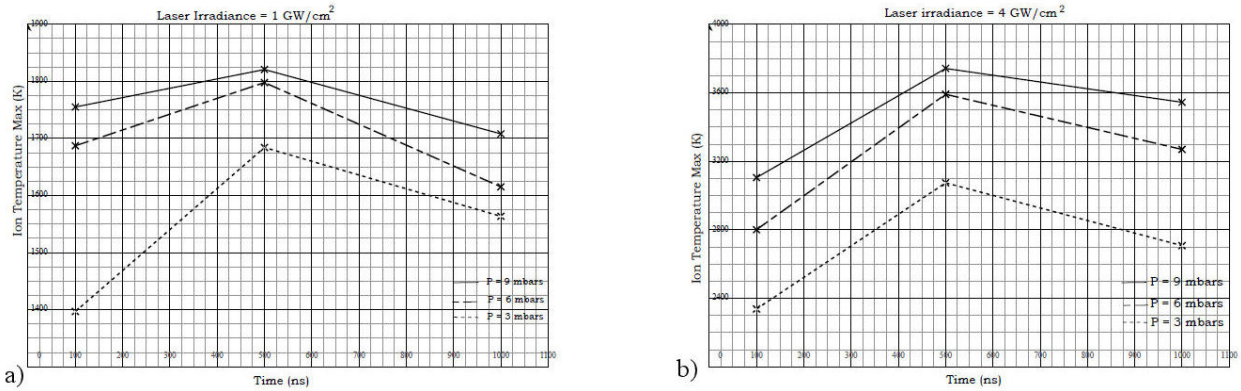

FIGURE 9. Variation of the ion temperature with the pressure (3 mbars dotted line, 6 mbars broken line and 9 mbars full line) at constant laser irradiance [a): 1 GW/cm^2, b) 4 GW/cm^2].

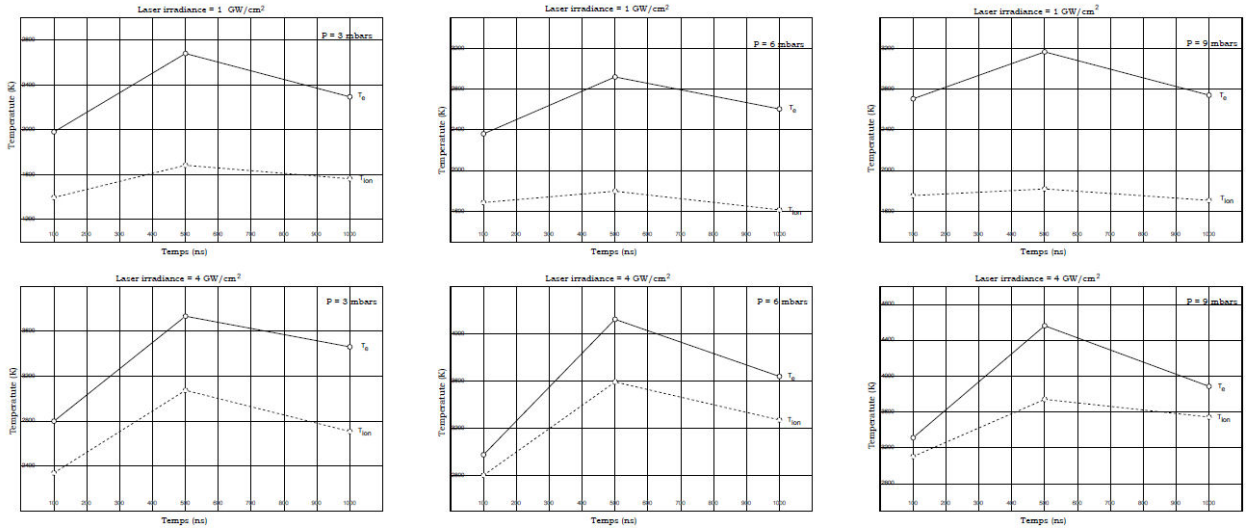

FIGURE 10. Comparison between electron temperature (full line) and the ion temperature (dotted line) for 3 dioxide carbon pressures: 3 mbars (1$^{\rm st}$ column), 6 mbars (2$^{\rm nd}$ column) and 9 mbars (3$^{\rm rd}$ column) at constant laser irradiance [1 GW/cm^2 (1$^{\rm st}$ row), 4 GW/cm^2 (2$^{\rm nd}$ row)].

3.3. Electron and ion number density

In this part, we consider, in our simulation model, a single laser beam with 4096 rays illuminating a spherical graphite target (radius = 0.05 cm, thickness = 0.05 cm) in 2D-cylindrical ($R-Z$) geometry. The laser is focused on the z-axis, and enters $R \in [0; 1.0\,\mathrm{cm}] \times Z \in [-0.4; 0.8\,\mathrm{cm}]$ computational domain at a 45° angle, the ambient gas is supposed to be CO_2 (Fig. 11). The boundary Conditions are set reflective for z-axis, whereas the remaining boundaries are set to outflow (zero gradient). We utilize 5 levels of refinement and blocks of 8×8 cells obtaining an equivalent resolution of 39 μm/cell.

Figures 12 and 13 show the electron and the ion density, respectively, for carbon dioxide pressure of 6 mbars and two laser irradiances 1 GW/cm^2 and 4 GW/cm^2 and three simulation times 100, 500 and 1000 ns. Each row in the figure shows the result obtained using one laser irradiance at 3 time steps. Each column shows the results for the same time for the two laser irradiances.

For all, the number density and the spatial extent of the corresponding profiles increase when the time step is increasing and with growing the laser irradiance. The peak of density for both electrons and ions is reached at 1000 ns.

3.4. Fluid velocity

Figure 14 shows time variation of the fluid velocity with the laser irradiance at constant pressure (6 mbar). For all simulations, the radial location of the shock front increases with laser irradiance, at the tree simulation times 100 ns, 500 ns and 1000 ns. The fluid velocity increases from 1.26×10^6 cm/s ($I = 1$ GW/cm^2) to 1.42×10^6 cm/s ($I = 4$ GW/cm^2) at $t = 100$ ns and from 7.55×10^5 cm/s ($I = 1$ GW/cm^2) to 8.32×10^5 cm/s ($I = 4$ GW/cm^2) at $t = 500$ ns and from 5.08×10^5 cm/s ($I = 1$ GW/cm^2) to 6.0×10^5 cm/s ($I = 4$ GW/cm^2) at $t = 1000$ ns. This phenomenon occurs due to the higher energy imparted to the target material by the more intense laser beam. When a laser, with higher irradiance, is employed, it delivers a greater amount of energy to the target

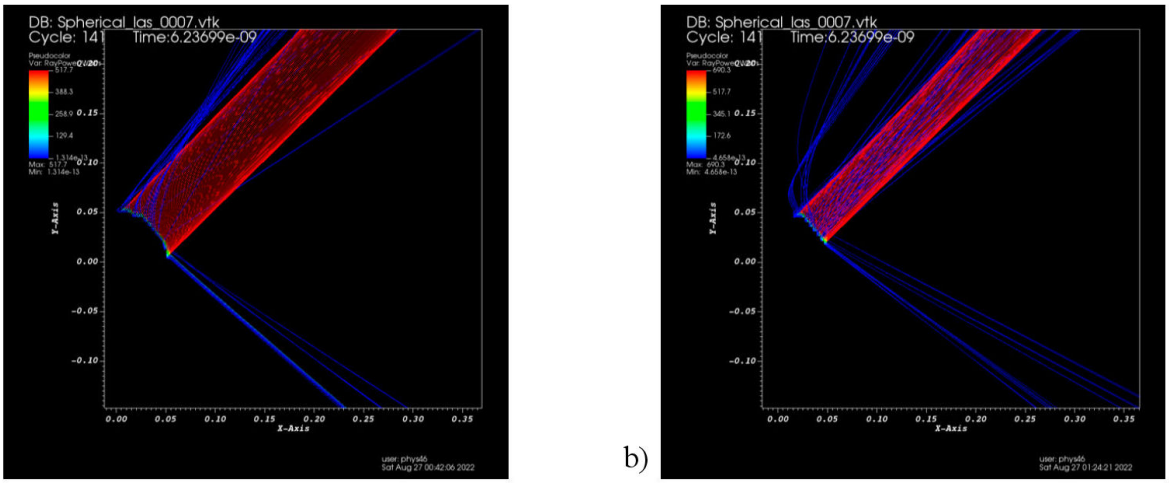

FIGURE 11. Laser beam simulated using 4096 rays per time step in 2D-cylindrical ($R-Z$) a) geometry for 1 GW/cm^2 and b) for 4 GW/cm^2.

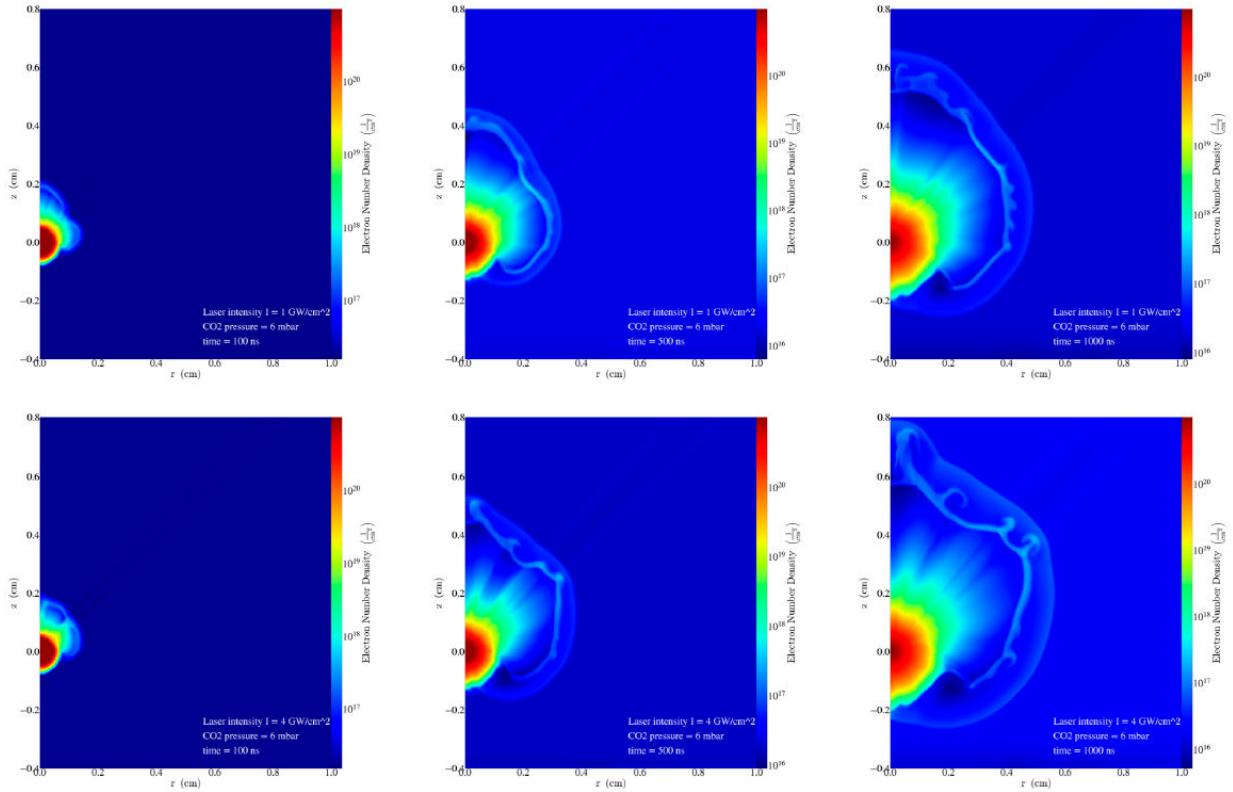

FIGURE 12. Electron density calculated at 6 mbars CO_2 ambient gas pressure, for 1 GW/cm^2, (1$^{\text{st}}$ row), 4 GW/cm^2 (2$^{\text{nd}}$ row) laser irradiance and for 3 time steps: 100 ns (1$^{\text{st}}$ column), 500 ns (2$^{\text{nd}}$ column) and 1000 ns (3$^{\text{rd}}$ column).

surface in a shorter period. Consequently, rapid heating and vaporization of the target material occur, leading to the formation of a plasma plume with higher kinetic energy. This phenomenon has been observed experimentally [47], and indicate the presence of a shock front associated with the plasma initiation, dynamics, and expansion into the ambient gas. As the plasma propagates a shock region of highly compressed gas is formed between the background gas and expanding plasma. Interaction of laser with the target results in the formation of plasma which is a strong source of UV radiation. In presence of an ambient gas this radiation interacts with it and results in an increase in the density in a very narrow region which propagates in the ambient atmosphere with speed more than that of the local ion sound speed [46]. laser interactions with solid density targets can be treated as a hydrodynamic problem with the laser rays acting as a source of energy on the grid. This laser energy is absorbed by electrons at a rate specified by the inverse bremsstrahlung approximation, after which this energy can be transferred to ions.

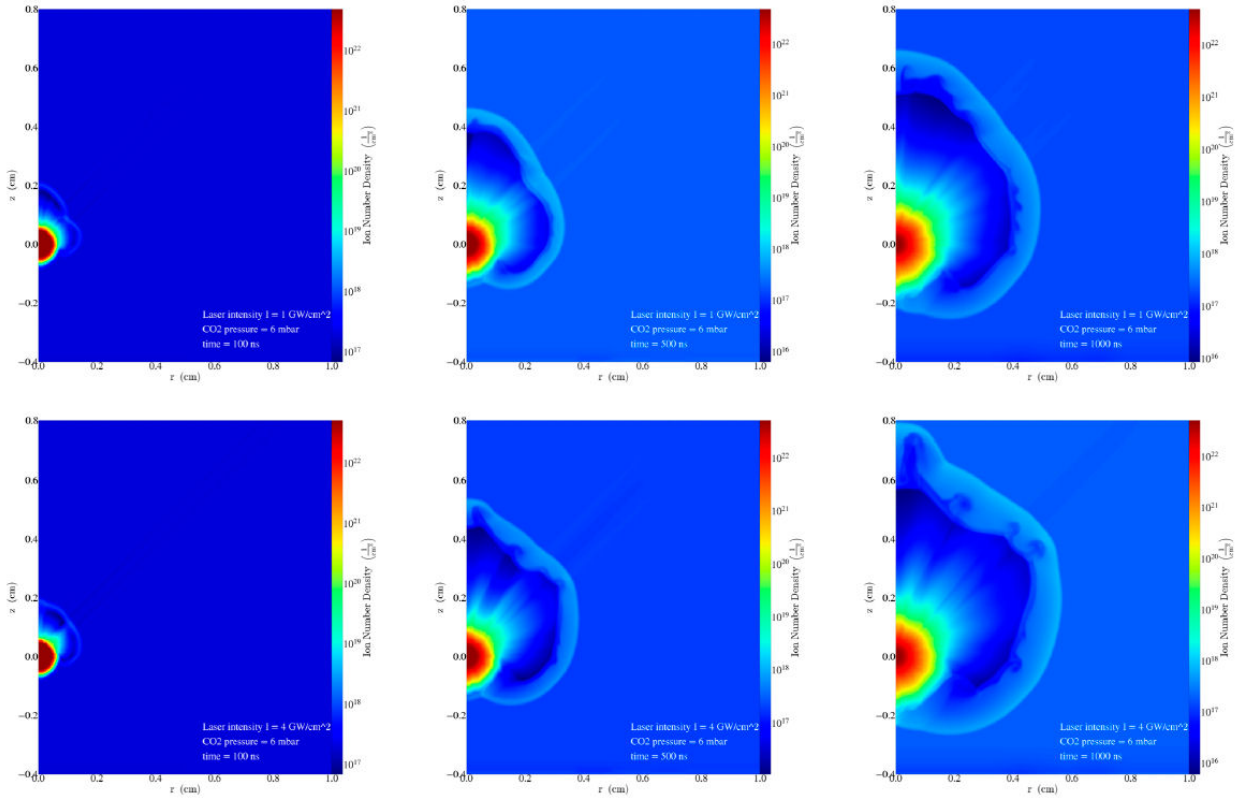

FIGURE 13. Ion density calculated at 6 mbars $C0_2$ ambient gas pressure, for 1 GW/cm^2, (1$^{\text{st}}$ row), 4 /cm^2 (2$^{\text{nd}}$ row) laser irradiance and for 3 time steps: 100 ns (1$^{\text{st}}$ column), 500 ns (2$^{\text{nd}}$ column) and 1000 ns (3$^{\text{rd}}$ column).

4. Limitation

The limitations of our approach, as highlighted in this study, primarily stem from our challenge to accurately determine the wide range of physical, chemical, optical, and environmental factors affecting plasma properties and the formation of spectral lines in Laser-Induced Breakdown Spectroscopy (LIBS). Initially, we simulate delay times of 100 ns, 500 ns, and 1000 ns; however, it is crucial to emphasize the importance of simulating early times (t = 10 ns), to understand the plasma formation dynamics when the pulsed laser interacts with the target is pivotal. Furthermore, the application of the hydrodynamics radiation model becomes unreliable during extended simulation periods, as the Knudsen Number (KN), which represents the ratio of species mean free path to plasma length, significantly increases. To address this challenge, alternative methodologies such as the direct simulation Monte Carlo approach can provide a more accurate depiction of plume expansion, particularly noticeable at prolonged delay times [48]. Additionally, employing a finer Eulerian grid in specific regions of the domain can yield more precise simulations, especially when considering the mixing between plasma formation and ambient gas. It is important to note that chemical reactions are not accounted for in this work, hence molecular band emissions are not considered. Molecular formation becomes particularly relevant at longer times [49].

5. Conclusion

This paper has provided detailed validation of a non-equilibrium model for laser-induced breakdown plasmas under Martian atmosphere conditions. Non-equilibrium effects were described using a 3T-Eurlian fluid model in the approximation that electrons and ions move together as a single fluid but with two different temperatures, and that this fluid can emit or absorb radiation. In our approach the atomic energy level populations were calculated using a collisional-radiative (CR) NLTE-model taking into account the mixing between the plasma and the ambiant gas. The simulation was performed with the FLASH radiation-hydrodynamics code which is a finite-volume Eulerian code that operates on a block-structured mesh using Adaptive Mesh Refinement (AMR). The plasma simulations were allowed to evolve for different times utilizing the second-order unsplit time marching method of USM algorithm.

We have investigated the effects of laser irradiance and ambient pressure on the plasma parameters namely the electron and ion temperatures and the electron and ion densities. We have also shown the temporal variation of the fluid velocity with the laser irradiance at constant pressure which indicated the presence of a shock front associated with the plasma initiation, dynamics, and expansion into the ambient gas.

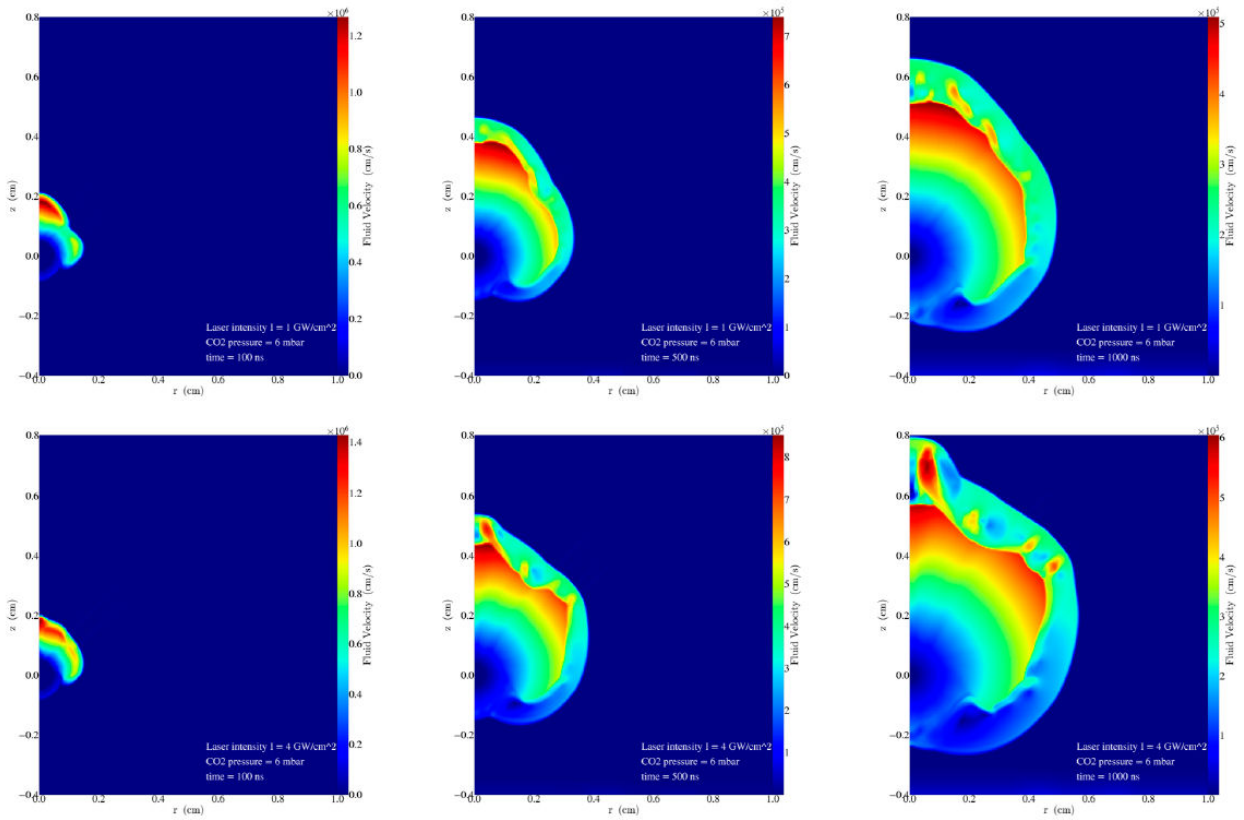

FIGURE 14. Fluid velocity calculated at 6 mbars $C0_2$ ambient gas pressure, for 1 GW/cm^2, (1$^{\rm st}$ row), 4 /cm^2 (2$^{\rm nd}$ row) laser irradiance and for 3 time steps: 100 ns (1$^{\rm st}$ column), 500 ns (2$^{\rm nd}$ column) and 1000 ns (3$^{\rm rd}$ column).

Appendix

A. Inverse Bremsstrahlung model used to calculate $Q_{\rm las}$

A.1 Ray-tracing in the geometric optics approximation to model laser energy deposition [33]

The laser beam is made of a number of rays whose paths are traced through the domain based on the local refractive index of each cell. The term represent the deposition of energy by laser heating. The laser power deposited in a cell is calculated based on the inverse Bremsstrahlung power in the cell and depends on the local electron number density gradient and local electron temperature gradient. The energy deposited by the laser beam was calculated using the laser ray trace approximation for planar and cylindrical geometries. In this approximation, the equation of motion of ray is given by:

$$\frac{d^2x}{dt^2} = \nabla\left(\frac{c}{2}\eta^2\right), \tag{A.1}$$

where the index of refraction η is given by:

$$\eta^2 = 1 - \frac{\omega_{\rm p}^2}{\omega^2} = 1 - \frac{n_{\rm e}}{n_{\rm c}}, \tag{A.2}$$

$$n_{\rm c} = \left(\frac{m_{\rm e}}{4\pi}\right)\left(\frac{\omega}{e}\right)^2, \tag{A.3}$$

where $\omega_{\rm p}$ is the plasma frequency, ω is the laser frequency, c is the speed of light in vacuum and $n_{\rm c}$ is the critical density at which the laser frequency and the plasma frequency are equal. The quantities $n_{\rm e}$, $m_{\rm e}$ and e are the density, the mass and the charge of the electron, respectively. Combing Eq. (A.1) with Eq. (A.2) we obtain the final from of the ray equation of motion:

$$\frac{d^2x}{dt^2} = \nabla\left(\frac{c^2}{2}\frac{n_{\rm e}}{n_{\rm c}}\right). \tag{A.4}$$

The electron number density is given by:

$$n_{\rm e}(\overrightarrow{x}) = \langle n_{\rm e}\rangle + \left\langle \overrightarrow{\nabla} n_{\rm e}\right\rangle .(\overrightarrow{x} - \langle\widehat{x}\rangle) + O(\varepsilon^2), \tag{A.5}$$

where $\langle\rangle$ denotes a zone average. The ray equation of motion Eq. (3) becomes:

$$\frac{d^2x}{dt^2} = -\left(\frac{c^2}{2}\right)\frac{\langle n_{\rm e}\rangle}{n_{\rm c}}. \tag{A.6}$$

This shows that when $n_{\rm e}$ is linear within a cell, the rays follow a parabolic trajectory through the cell. The electron number density will not be continuous in general. The Kaiser algorithm fixes this by applying Snell's law at the cell inter-

faces as the following equations :

$$\eta \sin\theta = \eta' \sin\theta', \tag{A.7}$$

$$\sqrt{1-\frac{n_{\rm e}}{n_{\rm c}}}\sin\theta = \sqrt{1-\frac{n'_{\rm e}}{n_{\rm c}}}\sin\theta', \tag{A.8}$$

where unprimed (primed) quantities denote values before (after) the transition, and θ is the angle between the ray velocity and the interface normal. This, rays can reflect or refract off of cell interface.

A.2 Power deposition by inverse Bremssrahlung [33]

Because rays are simply curves in space, they carry no information about radiation intensity or special extent transverse to their direction. Their state is completely defined by their frequency, velocity, and power, the latter two attributes of which are, in general, spatially dependent. The power P of an electromagnetic wave is depleted by the inverse Bremsstrahlung (*ib*) process.

The rate of power loss is governed by the 1^{st} order ordinary differential equation (ODE):

$$\frac{dP}{dt} = -\nu_{ib}(t)P. \tag{A.9}$$

As a ray travels through a cell, its power (energy) decreases with time:

$$P(\Delta t) = P_0 \exp - \left(\int_0^{\Delta t} \nu_{ib}(\overrightarrow{x}(t))dt \right). \tag{A.10}$$

The inverse Bremsstrahlung frequency factor ν_{ib} (the rate of energy loss) is given by the formula:

$$\nu_{ib} = \frac{n_{\rm e}}{n_{\rm c}}\nu_{ei}, \tag{A.11}$$

where ν_{ei} is the electron-ion collision frequency, given by :

$$\nu_{ei} = \frac{4}{3}\sqrt{\frac{2\pi}{m_e}}\frac{n_e \overline{Z} e^4 \ln\Lambda_{ei}}{(k_{\rm B}T_e)^{3/2}}. \tag{A.12}$$

Here $\overline{Z}$ is the average ionization number of the plasma, m_e, e and T_e are the mass, the charge and the temperature oh the electron respectively, $K_{\rm B}$ is the Boltzmann constant. The Coulomb logarithm $\ln\Lambda_{ei}$ is the natural logarithm of the Debye number and is taken here as:

$$\ln\Lambda_{ei} = \ln\left[\frac{3}{2\overline{Z}e^3}\sqrt{\frac{K_{\rm B}^3 T_e^3}{\pi n_e}}\right]. \tag{A.13}$$

The inverse Bremsstrahlung frequency depends thus on the electron temperature and the electron number density, both of which are functions of the position, and since the position changes with time, it's ultimately also a function of time:

$$\nu_{ib}(t) = \frac{4}{3}\sqrt{\frac{2\pi}{m_e}}\frac{\overline{Z}e^4}{n_c K_{\rm B}^{3/2}}\frac{n_e(x(t))^2 \ln\Lambda_{ei}(x(t))}{T_e(x(t))^{3/2}}. \tag{A.14}$$

B. CR NLTE - Model

To describe the population of the atomic levels, we utilized a collisional-radiative (CR) NLTE-model, which is equally applicable for low, and high temperature ranges. The number density of i-fold ionized ion n_i is given by NLTE rate equation (steady state):

$$n_{i+1}n_e^2\alpha_{i+1} + n_{i+1}n_e\beta_{i+1} + n_{i+1}n_e D_{i+1} - n_i n_e C_i = 0, \tag{B.1}$$

where α_{i+1}, β_{i+1} and D_{i+1} are the coefficients for collisional recombination, radiative and dielectronic recombination respectively. Collisional recombination is 3-body process involving two electrons and an ion. C_i denotes the electronic collisional ionization coefficient. The electron density is denoted by n_e and the ion density for the element under consideration in the mixture is $n_m = \sum_i n_i$.

The steady state solution of Eq. (B.1) gives the ion densities as:

$$\frac{n_{i+1}}{n_i} = \frac{C_i}{n_e\alpha_{i+1} + \beta_{i+1} + D_{i+1}}. \tag{B.2}$$

The above equations together with the consistency condition $n_m = \sum_i n_i$ is solved to obtain all n_i and the average degree of ionization.

All the coefficients for collisional recombination, radiative, dielectronic recombination and the electronic collisional ionization formula are described in Ref. [18].

Acknowledgments

One of the authors Pr Z. Bedrane gratefully acknowledges the DGRSDT, Algerian Ministry of Higher Education and Research, under Project PRFU code B00L02UN130120220002.

1. Mars exploration program, Curiosity Rover Mission Overview. https://mars.nasa.gov/msl/mission/overview/.

2. C. Fabre and B. Bousquet, *De ChemCam á SuperCam: l'apport de la LIBS pour le spatial, Photoniques* **103 2020**, https://doi.org/10.1051/photon/202010338.

3. K.A. Farley **et al**. Mars 2020 Mission Overview, *Space Sci Rev*, **216** (2020) 142, https://doi.org/10.1007/s11214-020-00762-y.

4. F. Colao, R. Fantoni, V. Lazic, and A. Paolini, LIBS applica-

tion for analyses of Martian crust analogues:search for the optimal experimental parameters in air and CO_2 atmosphere, *Appl. Phys. A*, **79** (2004) 143, https://doi.org/10.1007/s00339-003-2262-x.

5. M. Capitelli, A. Casavola, G. Colonna and A.D. Giacomo, Laser-induced plasma ex- pansion: theoretical and experimental aspects, *Spectrochim. Acta B At. Spectrosc.*, **59** (2004) 271, https://doi.org/10.1016/j.sab.2003.12.017.
6. A. Cousin *et al*., Laser induced breakdown spectroscopy library for the martian environment, *Spectrochim. Acta B At. Spectrosc.*, *66* (2011) 805, https://doi.org/10.1016/j.sab.2011.10.004.
7. J. Colgan *et al*., Theoretical modeling and analysis of the emission spectra of a ChemCam standard: basalt BIR-1A, *Spectrochim. Acta B At. Spectrosc. 110* (2015) 20, https://doi.org/10.1016/j.sab.2015.05.005.
8. E. Ewusi-Annan, D. M. Surmick, N. Melikechi and R.C. Wiens, Simulated laser-induced breakdown spectra of graphite and synthetic shergottite glass under Martian conditions, *Spectrochimica Acta Part B, 148* (2018) 31, https://doi.org/10.1016/j.sab.2018.06.006.
9. P. B. Hansen, S. Schröder, S. Kubitza, K. Rammelkamp, D. S. Vogt, and H.-W. Hübers, Modeling of time-resolved LIBS spectra obtained in Martian atmospheric conditions with a stationary plasma approach, *Spectrochimica Acta Part B: Atomic Spectroscopy, 178* (2021) 106115, https://doi.org/10.1016/j.sab.2021.106115.
10. G. Cristoforetti *et al*., Local thermodynamic equilibrium in laser-induced breakdown spectroscopy: beyond the McWhirter criterion, *Spectrochim. Acta - Part B At. Spectrosc.*, **65** (2010) 86, https://doi.org/10.1016/j.sab.2009.11.005.
11. A. Alberti *et al*., Laser-induced non-equilibrium plasma kernel dynamics, *J. Phys. D: Appl. Phys.*, **53** (2020) 025201, https://doi.org/10.1088/1361-6463/ab492a.
12. N. G. Glumac and G. S. Elliott, The effect of ambient pressure on laser-induced plasmas in air, *Opt. Lasers Eng.*, **45** (2007) 27, https://doi.org/10.1016/j.optlaseng.2006.04.002.
13. N. Tsuda and J. Yamada, Observation of forward breakdown mechanism in high-pressure argon plasma produced by irradiation by an excimer laser, *J. Appl. Phys.*, **81** (1996) 96, https://doi.org/10.1063/1.364200.
14. J. Macfarlane, I. Golovkin, and P. Woodruff, HELIOS-CR - A 1-D radiation-magnetohydrodynamics code with inline atomic kinetics modeling, *J. Quant. Spectrosc. Radiat. Transf.*, **99** (2006) 381, https://doi.org/10.1016/j.jqsrt.2005.05.031.
15. The Flash Center for Computational Science, *FLASH User's Guide Version-4.6.2*, University of Rochester, (2019). https://flash.rochester.edu/site/flashcode/user_support/.
16. P. MacNeice, K. M. Olson, C. Mobarry, R. De Fainchtein and C. Packer, PARAMESH: A parallel adaptive mesh refinement community toolkit, *Computer Physics Communications 126* (2000) 330, https://doi.org/10.1016/S0010-4655(99)00501-9.
17. C. Orban, Fatenejad M., Chawla S., Wilks S. and Lamb D., A Radiation-Hydrodynamics Code Comparison for Laser-Produced Plasmas: FLASH versus HYDRA and the Results of Validation Experiments, *LLNL-JRNL:Physics.plasm-ph*, **7** (2013) 636375, https://doi.org/10.48550/arXiv.1306.1584.
18. J.J. MacFarlane, IONMIX-a code for computing the equation of state and radiative properties of LTE and non-LTE plasmas, *Comput. Phys. Comm.*, **56** (1989) 259, https://doi.org/10.1016/0010-4655(89)90023-4.
19. D. Lee, A solution accurate, efficient and stable unsplit staggered mesh scheme for three dimensional magnetohydrodynamics, *J. Comput. Phys.*, **243** (2013) 269, https://doi.org/10.1016/j.jcp.2013.02.049.
20. P. Colella, Multidimensional upwind methods for hyperbolic conservation laws, *J. Comput. Phys.* **87** (1990) 171, https://doi.org/10.1016/0021-9991(90)90233-Q.
21. S. Li, An HLLC Riemann solver for magneto-hydrodynamics, *J. Comput. Phys.*, **203** (2005) 344, https://doi.org/10.1016/j.jcp.2004.08.020.
22. The HYPRE library is available at: https://computing.llnl.gov/projects/hypre-scalable-linear-solvers-multigrid-methods/software.
23. D. Mihalas and B. W. Mihalas, Foundations of radiation hydrodynamics, *Oxford University Press*, New York, (1984) ISBN 0-19-503437-6.
24. J. I. Castor, Radiation Hydrodynamics, *Cambridge University Press*, (2004). ISBN: 9780511536182.
25. L. Spitzer, Physics of Fully Ionized Gases, *Interscience Publishers*, New York, (1962) ISNB: 3-978-0486449821.
26. S. Atzeni and J. Meyer-Ter-Vehn, The Physics of Inertial Fusion: Beam Plasma Interaction, Hydrodynamics, Hot Dense Matter, *International Series of Monographs on Physics, Oxford University Press*, (2004) ISBN 9780198562641.
27. H. Brysk, P.M. Campbell, and P. Hammerling, Thermal conduction in laser fusion, *Plasma Phys.*, **17** (1974) 473, https://doi.org/10.1088/0032-1028/17/6/007.
28. The Flash Center for Computational Science, available online https://flash.rochester.edu/
29. P. Tzeferacos *et al*., FLASH MHD simulations of experiments that study shock-generated magnetic fields, *High Energy Density Phys.*, **17** (2015) 24, https://doi.org/10.1016/j.hedp.2014.11.003.
30. B. Fryxell *et al*., FLASH: An adaptive mesh hydrodynamics code for modeling astrophysical thermonuclear flashes, *The Astrophysical Journal Supplement Series*, **131** (2000) 273, https://doi.org/10.1086/317361.
31. D. Lee and A. E. Deane, An unsplit staggered mesh scheme for multidimensional magnetohydrodynamics, *J. Comput. Phys.*, **228** (2009) 952, https://doi.org/10.1016/j.jcp.2008.08.026.
32. M. M. Marinak *et al*., NP8.00100: New capabilities in HYDRA for simulations of inertial confinement fusion targets, in 51st Annual Meeting of the APS Division of Plasma Physics (American Physical Society, 2009), **Vol. 54** p. 15. Site: https://meetings.aps.org/Meeting/DPP09/Content/1617.

33. T.B. Kaiser, Laser ray tracing and power deposition on an unstructured three- dimensional grid, *Phys. Rev. E*, **61** (2000) 895, https://doi.org/10.1103/PhysRevE.61.895.

34. A. Kramida, Yu. Ralchenko, and J. Reader, NIST ASD Team, NIST Atomic Spectra Database (ver. 5.9), [Online]. Available: https://www.nist.gov/pml/atomic-spectra-database.

35. S. Acquaviva and M. L. D. Giorgi, High-resolution investigations of C_2 and CN optical emissions in laser-induced plasmas during graphite ablation, *J. Phys. B Atomic Mol. Phys.*, **35** (2002) 795, https://doi.org/10.1088/0953-4075/35/4/304.

36. S. Maurice *et al.*, The ChemCam instrument suite on the Mars science laboratory (MSL) rover: science objectives and mast unit description, *Space Sci. Rev.*, **170** (2012) 95, https://doi.org/10.1007/s11214-012-9912-2.

37. J. R. Davies *et al*., Laser entrance window transmission and reflection measurements for preheating in magnetized liner inertial fusion, *Physics of Plasmas*, **25** (2018) 062704, https://doi.org/10.1063/1.5030107.

38. A. J. Harvey-Thompson *et al*., Diagnosing laser-preheated magnetized plasmas relevant to magnetized liner inertial fusion, *Physics of Plasmas*, **22** (2015) 122708, https://doi.org/10.1063/1.4938047.

39. K. Gillen-Christandl, D. Gillen Glen, M. J. Piotrowicz and M. Saffman, Comparison of Gaussian and super Gaussian laser beams for addressing atomic qubits, *Appl. Phys. B*, **122** (2016) 131, https://doi.org/10.1007/s00340-016-6407-y.

40. R. J. LeVeque, Finite Volume Methods for Hyperbolic Problems, *Cambridge University Press*, (2002) ISBN: 9780511791253.

41. E.F. Toro, Riemann Solvers and Numerical Methods for Fluid Dynamics, *Springer Science & Business Media*, (2009) ISBN: 978-3-540-49834-6.

42. M. J. Turk, A multi-code analysis toolkit for astrophysical Simulation data, *The Astrophysical Journal Supplement Series*, **192** (2011) 16, https://doi.org/10.1088/0067-0049/192/1/9.

43. S.S. Harilal, C.V. Bindhu, R.C. Issac, V. P. N. Nampoori, and C. P. G. Vallabhan, Electron density and temperature measurements in a laser produced carbon plasma, *J. Appl. Phys.*, **82** (1997) 2140, https://doi.org/10.1063/1.366276.

44. T.A. Heltemes and G.A. Moses, BADGER v1.0: A Fortran equation of state library, *Computer Physics Communications* **183** (2012) 2629, https://doi.org/10.1016/j.cpc.2012.07.010.

45. Z. Chen, Z. Chen, W. Jiang, L. Guo, and Y. Zhang, Line intensity calculation of laser-induced breakdown spectroscopy during plasma expansion in nonlocal thermodynamic equilibrium, *Opt. Lett.* **48** (2023) 3227, https://doi.org/10.1364/OL.488250.

46. A.K. Sharma and R.K. Thareja, Plume dynamics of laser-produced aluminum plasma in ambient nitrogen, *Applied Surface Science* **243** (2005) 68, https://doi.org/10.1016/j.apsusc.2004.09.093.

47. T.E. Itina, J. Hermann, P. Delaporte, and M. Sentis, Laser-generated plasma plume expansion: combined continuous-microscopic modeling, *Phys. Rev. E 66* (2002) 066406, https://doi.org/10.1103/PhysRevE.66.066406.

48. M. Skocic and S. Bukvic, Laser induced plasma expansion and existence of local thermodynamic equilibrium, *Spectrochim. Acta B At. Spectrosc.* **125** (2016) 103, https://doi.org/10.1016/j.sab.2016.09.011.

49. M. Dong, J. Lu, S. Yao, Z. Zhong, J. Li and W. Lu, Experimental study on the characteristics of molecular emission spectroscopy for the analysis of solid materials containing c and n, *Opt. Express* **18** (2011) 17021, https://doi.org/10.1364/OE.19.017021.